Femto-Second Laser-Based Free Writing of 3D Protein Microstructures and Micropatterns with Sub-Micrometer Features: A Study on Voxels, Porosity, and Cytocompatibility

Barbara Pui Chan, Jiao Ni Ma, Jin Ye Xu, Chuen Wai Li, Jin Ping Cheng, and Shuk Han Cheng*

Femto-second laser-based free-writing of complex protein microstructures and micropatterns, with sub-micrometer features and controllability over voxel dimension, morphology, and porosity, is reported. Protein voxels including lines, spots, and micropillars are fabricated. Laser power, exposure time, z-position, protein and photosensitizer concentrations, but not scanning speed, are important controlling parameters. A lateral fabrication resolution of ≈200 nm is demonstrated in 2D line voxels. 3D spot voxels are ellipsoids with 400 nm lateral and 1.5 μm axial dimensions. An ascending z-stack scanning method to verify the theoretical axial optical resolution, delineate and enhance the axial fabrication resolution of 3D structures, including square prism and cylinder micropillars, is also reported. The micropillar array presents a simple "write-and-seed" and table platform for cell niche studies. Fibroblasts attach to, grow on, and express adhesion to molecules on micropillar arrays without the need of matrix coating. They exhibit a more "3D" morphology comparing with that in 2D monolayer cultures and physiological functions such as matrix deposition. This work presents an important milestone in engineering complex protein microstructures and micropatterns with sub-micrometer topological features to mimic the native matrix niche for cell-matrix interaction studies.

1. Introduction

Advancement in fabrication technologies such as ink-based writing,[1] holographic lithography,[2] and dip-pen technology[3] has enabled the fabrication of structures with micro- and nanosized features for microfluidics, microelectromechanical,[4] and biomedical[5] applications. Readers are directed to a few excellent reviews on these technologies.[6–8] Multiphoton absorption-based fabrication is an emerging technology utilizing femto-second lasers for free-form fabrication of structure with features of sub-diffraction limit down to 100 nm resolution.[6,9,10] This technology has particular advantages over traditional micro- and nanofabrication technologies for biomedical applications because the processing conditions are mild without the need to use harsh reagents such as organic solvents and sophisticated and expensive facilities such as clean rooms.

Multiphoton absorption is a phenomenon that happens when an atom absorbs two or more photons simultaneously, activating higher electronic states.[11] In contrast to single photon absorption, in which absorption and excitation occurs anywhere within the converging and diverging cones of the laser beam, multiphoton absorption; hence, excitation is only localized to the tiny focal volume of the laser beam.[11] This inherent spatial sectioning capability and the associated advantages such as attenuation of out-of-focus fluorophore bleaching, lower photocytotoxicity, excellent spatial resolution, and greater penetration depth make multiphoton absorption widely applied in fluorescence imaging for thick sections or even tissues when combining with confocal laser scanning microscopy.[11]

Apart from fluorescent imaging, multiphoton absorption starts to find its application in biofabrication. Multiphoton photopolymerization refers to the process in which monomers are polymerized upon multiphoton absorption of photoinitiators.[6,9] Multiphoton absorption-based photopolymerization of resins such as acrylate[12,13] and NOA61,[14] hydrogels such as poly(ethylene glycol),[15] and polydimethylsiloxane (PDMS)[16] have been reported. However, these platforms require time-consuming masking, curing, and development procedures, and have inherent cytocompatibility problems, therefore requiring coating of matrix proteins for cellular studies. Multiphoton photochemical crosslinking refers to the process in which protein materials are covalently crosslinked through photochemical reactions happened in the infrared spectral region. This process differs from photopolymerization because the solidification mechanism may not necessarily be polymerization. Proteins are important materials with excellent cytocompatibity

---

Dr. B. P. Chan, J. N. Ma, J. Y. Xu, C. W. Li
Tissue Engineering Lab
Department of Mechanical Engineering
The University of Hong Kong, Pokfulam Road,
Hong Kong Special Administrative Region, China
E-mail: bpchan@hku.hk
Dr. J. P. Cheng, Prof. S. H. Cheng
Department of Biology and Chemistry
City University of Hong Kong
Hong Kong Special Administrative Region, China.

DOI: 10.1002/adfm.201300709

© 2013 WILEY-VCH Verlag GmbH & Co. KGaA, Weinheim

for biomedical applications. Complex structures and patterns made by protein materials with micro- and nano-features are essential for engineering complex biomimetic matrix for cell niche studies. Multiphoton absorption-based photochemical crosslinking has been reported to crosslink a wide range of naturally occuring proteins such as fibrinogen and alkaline phosphatase,[17–19] glutamate dehydrogenase,[20] bovine serum albumin (BSA),[17–22] and collagen.[23] Protein lines have been fabricated to guide neurite growth of neuronal cells,[20] and to study cellular activities, including fibroblast adhesion[24] and cancer cell migration.[25] Protein cables, pads, and rectangular matrices were fabricated and functionalized with chemicals such as enzymes[26] or dyes,[18,19] generating concentration gradients for controlled release purposes. Multiphoton-based fabrication of 3D protein microstructures including arch constructs for stem cell migration study,[27] circular enclosures, and bendable rods with chemical responsiveness to pH and ion-strength changes[28] for microfluidic applications such as bacteria capturing and steering,[29] tunable protein microlenses with highly smooth surfaces and excellent optical properties as potential organic optical microdevices,[21,22] have been reported. Complicated 3D protein structures can be made using a digital micromirror device-directed masking,[30] leading to the fabrication of protein microchambers trapping bacteria and yeasts,[31] strongly suggesting the potential of using multiphoton-based protein photochemical crosslinking to engineer complex cellular microenviornments or niches consisting of multiple signals including soluble factors, extracellular matrix, topological features, and mechanical information. In order to engineer complex cell microenvironment with precise controllability, thorough understanding of the protein voxels, the controllability of their dimension and morphology, the relationship between theoretical optical resolution and the practical fabrication resolution is essential. Nevertheless, studies of this kind are lacking. Moreover, multiphoton photopolymerized materials are usually non-porous but microporous structures and patterns are more relevant and preferred in biomedical applications.[32] As a result, investigating whether multiphoton photochemical crosslinking controls the porosity of protein structures is also essential to fabricating protein structures with controllable mechanical properties and soluble factor eluting properties. Finally, the stability of multiphoton photochemical crosslinking-based protein structures such as micropillar arrays under culture conditions and the cytocompatibility of protein micropillar arrays without matrix coating have not been studied.

In this study, we use dual photon confocal scanning microscopy as the light source and the scanning system, BSA as the sample protein, and rose Bengal (RB) a clinically used vital dye as the photosensitizer. We fabricated a wide range of protein microstructures and micropatterns with sub-micrometer features including sub-micrometer suspending bridges on micropiers and arrays of pyramid or cylindrical micropillars. We conducted detailed voxel study by fabricating protein line, spot, and micropillar voxels using different scanning modes, and investigated the dependence of voxel dimension on various controlling parameters including laser power, exposure time, scan speed, step size, and concentrations of BSA and RB. We also developed a novel method, namely, ascending z-stack scan, to study voxel morphology and dimension, to verify the theoretical optical resolution and to delineate the relationship between the planned step size and the axial fabrication dimension of voxels. Moreover, we investigated the porosity of protein matrices fabricated by frame scan and delineated the major controlling parameters for porosity. Finally, we tested the stability of micropillar arrays under culture conditions and investigated the cytocompatibility of protein micropillar arrays without matrix coating using fibroblasts as the sample cell system. Our results demonstrated that multiphoton-based photochemical crosslinking is a versatile micro- and sub-micrometer-fabrication technology for protein structures with controllable voxel morphology, dimension, and porosity. The fabricated arrays of protein micropillars of different morphologies with sub-micrometer features represent an excellent micropatterned cell culture system with simple and rapid “write-and-seed” fabrication procedure, good stability, and superb cytocompatibility, such that cells can attach and survive without any specific matrix coating. This work contributes to precise engineering of 3D complex and user-defined protein structures and patterns with sub-micrometer features for biomedical applications, such as screening multiple niches including matrix, topological and mechanical signals that determine stem cell fates.

2. Results

2.1. Two-Photon Fabrication of a Wide Spectrum of 3D Protein Microstructures and Micropatterns with Sub-Micrometer Features

Using two-photon confocal laser scanning at 800 nm and a solution containing BSA and RB, we demonstrated the capability to fabricate a wide spectrum of user-defined real 3D protein microstructures and micropatterns with sub-micrometer features. **Figure 1** shows the fluorescent and scanning electron microscopy (SEM) images of parallel lines (Figure 1A,B), rectangular matrix (Figure 1C,D), freely-written letters (Figure 1E,F), microwell (Figure 1G,H), arrays of micropillars in the shape of pyrimids (Figure 1I,J), square prism and cylinders (Figure 1K,L), and complex structures consisting of block and trapezoid piers with nanosized suspended bridge (Figure 1M,Q). Three micrometer-sized square-based piers (4 µm × 4 µm) were fabricated first and were interconnected by two nanosized (<800 nm width x < 800 nm thickness) double-layer suspending bridges (Figure 1M,N). The interlayer interval was around 750 nm (Figure 1O). The central square-based pier was also connected with a trapezoidal pier (4 µm × 4 µm at base and 1 µm × 1 µm at top) by another nanosized suspending bridge (<600 nm width x < 1 µm thickness) (Figure 1P,Q). The current study focuses on pixel analysis of protein lines, spots and micropillars, and porosity analysis of rectangular matrices.

2.2. Voxel Study of Protein Lines

2D lines are the simplest voxel structures for lateral resolution determination. **Figure 2** shows single pixel-wide protein lines fabricated by line scanning with increasing laser power (Figure 2A) and increasing number of scanning cycles (Figure 2B).

© 2013 WILEY-VCH Verlag GmbH & Co. KGaA, Weinheim

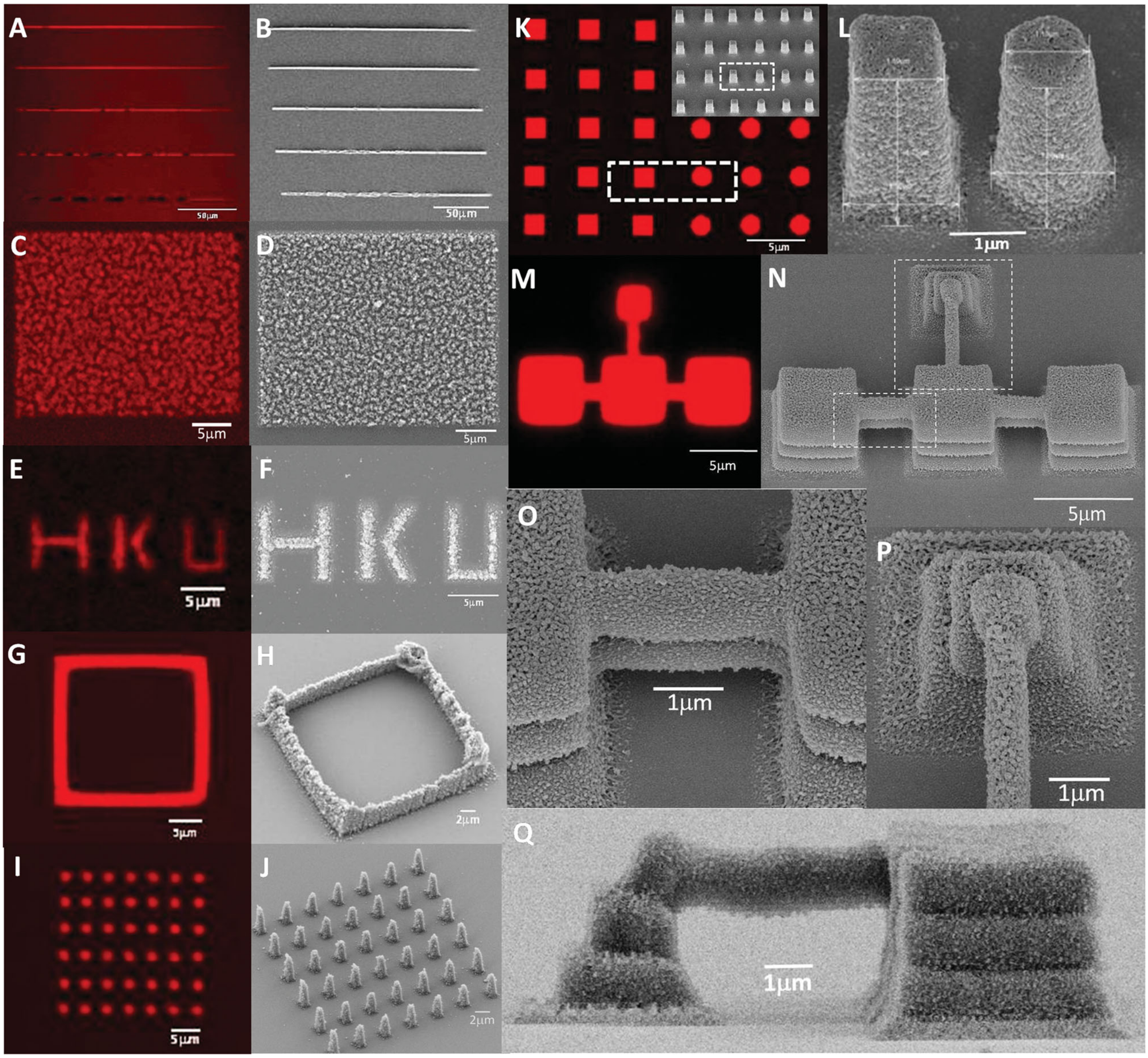

Figure 1. 3D protein microstructures and micropatterns fabricated by two-photon photochemical crosslinking. A,C,E,G,I,K,M) Fluorescent images taken immediately after fabrication; B,D,F,H,J,L,N,O,P,Q) SEM images. A,B) Lines (scale bar: 50 μm); C,D) Rectangular matrix (scale bar: 5 μm); E,F) "HKU" letters (scale bar: 5 μm); G,H) Microwell (scale bar: 5 μm for G and 2 μm for H); I,J) Pyrimidal micropillar array (scale bar: 5 μm for (I) and 2 μm for (J)); K) Fluorescent image of an array of square prisms and cylinders (scale bar: 5 μm) with low magnification SEM image as the insert; L) High magnification SEM images of a square prism (left) and a cylinder (right) (scale bar: 1 μm); M,N) A complex structure with three square-based bridge piers interconnected with two suspended double-layered bridges while the central pier was connected with a trapezoidal prism via a slender suspended bridge (scale bar: 5 μm, dotted lines: see (O,P)); O: Magnified view of the square-based piers with the double-layered suspending bridges (scale bar: 1 μm); P) Magnified view of the trapezoidal pier and the suspended bridge (scale bar: 1 μm); Q) Side view of the pier-bridge structure (scale bar: 1 μm).

Increasing lateral dimension or width of the protein lines, ranging from ≈200 nm to >600 nm has been demonstrated as the laser power increased from 24 to 40 mW (Figure 2A1,2). A strong positive linear relationship, representing a statistically significant linear regression coefficient of 0.965 ($p < 0.001$), between the protein line width and the laser power, was detected (Figure 2A3) with an excellent fitting, representing a coefficient of determination (R^2_{linear}) of 0.931. Figure 2B1,2 showed that the width of protein lines increased from ≈250 nm to ≈650 nm as the number of scanning cycles increased from 50 to 600 cycles, equivalent to increasing exposure time from 0.08064 to 0.96768 s. The relationship between the protein line width and the number of scanning cycles is also positive and strong but is nonlinear, as saturation has been found at 500 scanning cycles, corresponding to 0.8064 s of exposure time. The nonlinear association is statistically significant with a quadratic regression coefficient of 0.942 ($p < 0.001$), while the nonlinear fitting is very good with a coefficient of determination ($R^2_{\text{quadratic}}$) of 0.887.

© 2013 WILEY-VCH Verlag GmbH & Co. KGaA, Weinheim

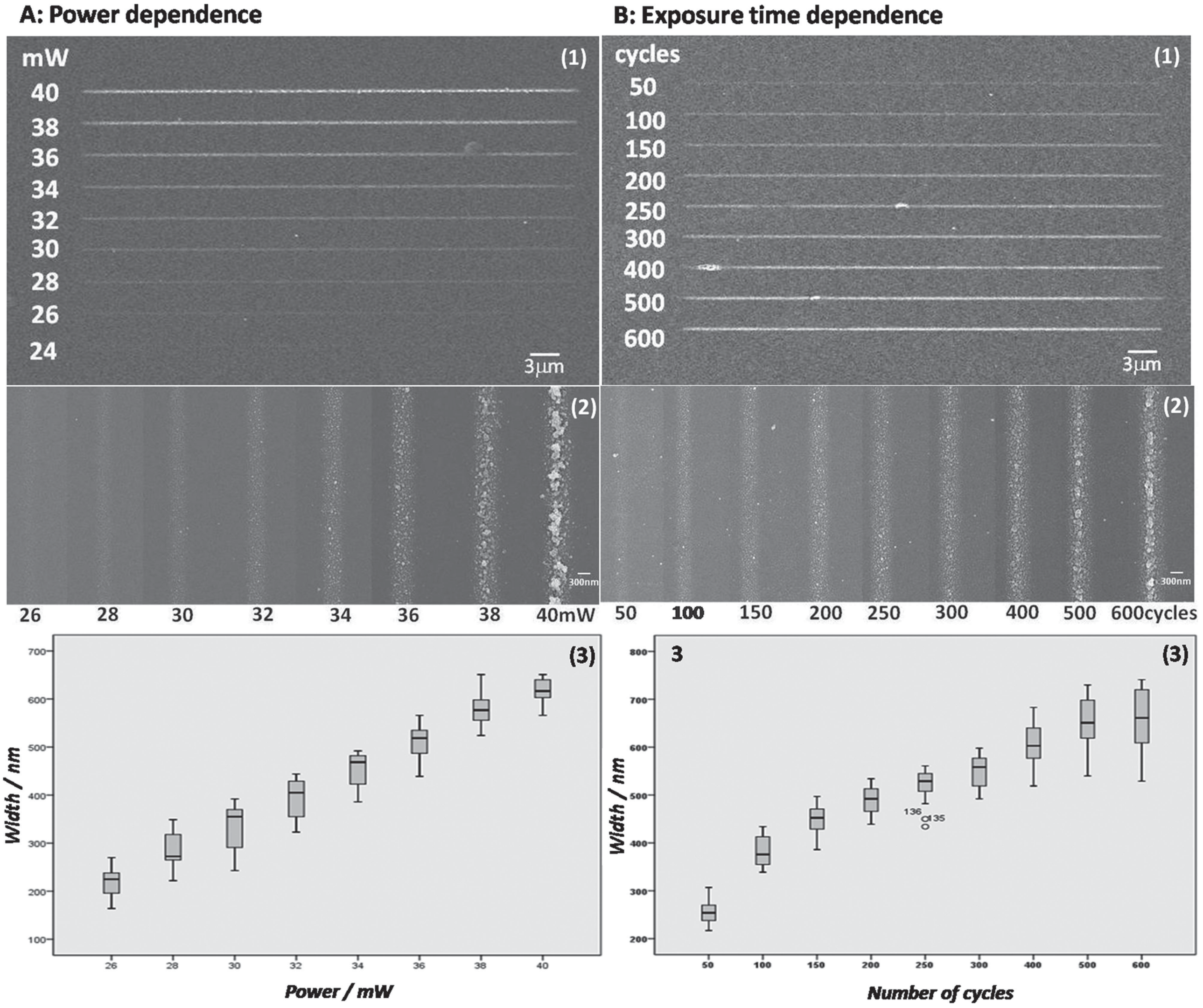

Figure 2. Power and scanning cycle dependence of protein line width. BSA protein lines were fabricated by repeated line scan. A) Power dependence ranging from 24 to 40 mW at 100 scanning cycles. 1) Low magnification (1.5 KX, scale bar: 3 μm) and 2) high magnification (25 KX, scale bar: 300 nm) SEM images; 3) box plot of line width against power ($R^2_{\text{linear}} = 0.931$, $p < 0.001$) ($n = 3$). B) Scanning cycle dependence ranging from 50 to 600 scanning cycles, equivalent to 0.08064 to 0.96768 s of exposure time, at 30 mW. 1) Low magnification (1.5 KX, scale bar: 3 μm) and 2) high magnification (25 KX, scale bar: 300 nm) SEM images; 3) box plot of line width against number of scanning cycle ($R^2_{\text{quadratic}} = 0.887$, $p < 0.001$) ($n = 3$).

2.3. Voxel Study of Protein Spots

Protein spots are the simplest structures for studies of 3D voxel morphology and fabrication resolutions. **Figure 3** shows single protein spot voxels fabricated by spot scanning. The morphology and dimension of protein spots was highly controlled by parameters including laser power (Figure 3A,E), exposure time (Figure 3B,F), and *z*-position for fabrication (Figure 3D,H), but is independent of laser scanning speed (Figure 3C,G). The width of the cone-like protein spots increased from ≈500 nm to ≈1 μm as the power increased from 28 to 36 mW and leveled off thereafter while the height increased from <1 μm to ≈4 μm as the power increased from 28 to 40 mW without saturation. The corresponding aspect ratio (AR) of the spot voxel also increased from 1.5 to 3.5 at ascending power. Linear regression analysis showed that width, height, and AR of spot voxel significantly associate with laser power in a linear manner ($p < 0.001$ for all) with moderate yet meaningful fitting, in terms of coefficients of determination (R^2) of 0.483, 0.552, and 0.529, respectively. Figure 3B,F shows the dependence of spot voxel dimensions on the exposure time between 1.21 to 48.41 s, controlled through varying number of scan cycles ranging from 10 to 400. The width of the cone-like protein spots increased from ≈500 nm to 1 μm at 12.10 s and leveled off thereafter while the height increased in a similar manner from ≈1 μm to ≈3 μm before saturation. The corresponding AR also increased from 1.5 to >3.5 before saturation. Regression analysis showed that all dimensions of the protein spots significantly associate with the exposure time ($p < 0.001$). Although linear regression coefficients for all dimensions were statistically significant, nonlinear

© 2013 WILEY-VCH Verlag GmbH & Co. KGaA, Weinheim

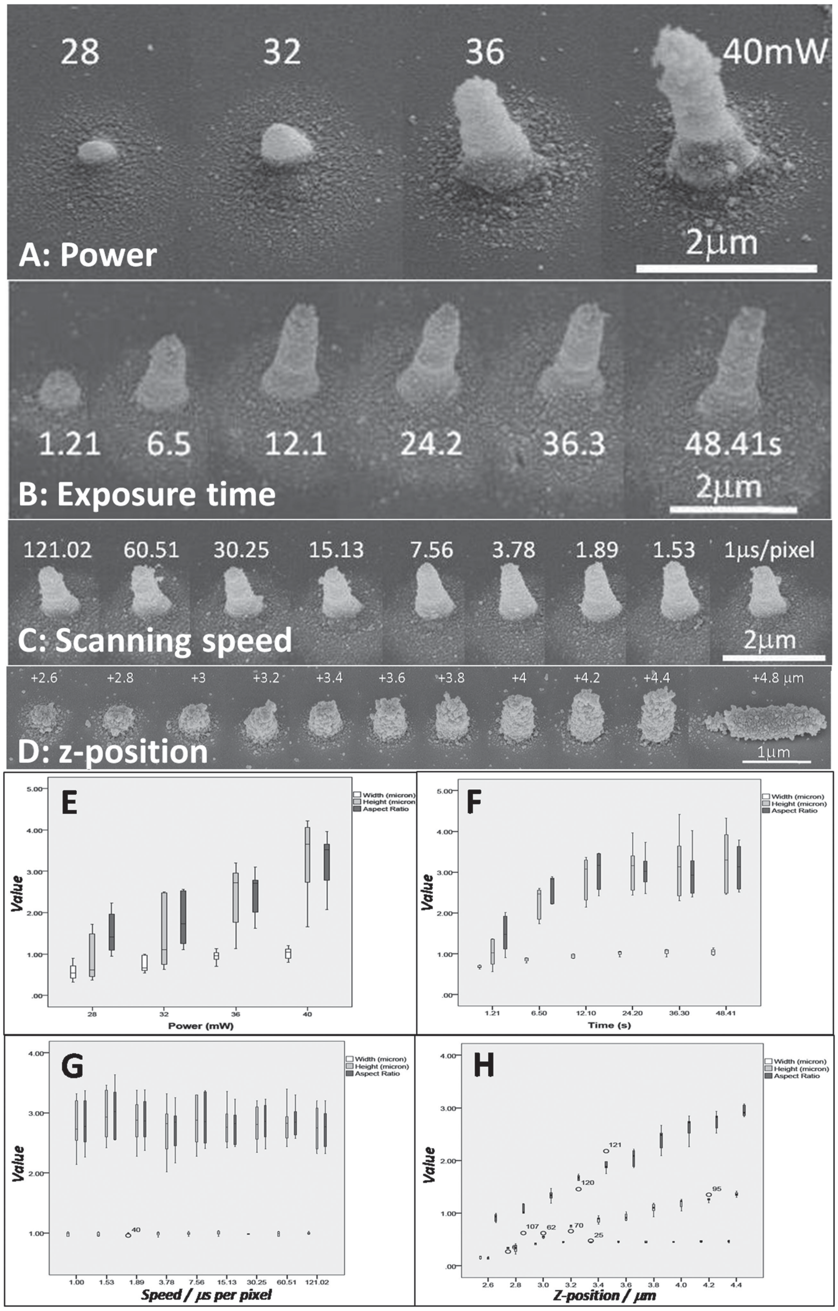

Figure 3. Protein spot voxel analysis on dimension and morphology. Protein spots were fabricated by time series scan under spot mode scanning. A–D) SEM images (scale bar: 2 μm for (A–C) and 1 μm for (D). E–H) Box plot showing the relationship between spot voxel dimensions (width, height, and aspect ratio) and different controlling parameters. A,E) Power dependence ($n = 7$). B,F) Exposure time dependence ($n = 6$). C,G) Scanning speed dependence ($n = 6$). D,H) Z-position dependence ($n = 5$).

relationship showed even better fitting with larger coefficients of determination (R^2) of 0.594, 0.821, and 0.463, respectively. Total exposure time can be controlled through varying the number of scanning cycles and the scanning speed, which defines the dwelling time per pixel. For the same scanning cycle, a lower scanning speed means a shorter dwell time per pixel, and hence a longer exposure time. As a result, the protein spot dimension increased with decreasing scanning speed when the number of scanning cycle is constant (data not shown). However, the real effect of scanning speed can only be determined by fixing the exposure time, through adjusting the number of scanning cycles. Figure 3C,G shows that all cone-like spot voxels have similar dimensions as the scanning speed increased from 1.0 to 121.02 μs pixel^{-1}, at a constant exposure time of 12 s. Linear regression analysis showed that all voxel dimensions have no significant association with the scanning speed ($p > 0.05$ for all). Z-position for fabrication defines the initial position where scanning starts. Ascending z-position from below the substrate–solution interface to where a whole single voxel was fabricated has been used to study voxel morphology in polymers.[13] In order to determine the fabrication resolution, small voxels are usually fabricated using close-to-threshold parameters.[13,33] In the protein spot study, small single protein spot voxels were fabricated (Figure 3D) using very low laser power at 15 mW and a single scanning cycle, at ascending z-positions from –1.0 to +4.8 μm. Figure 3H shows that the lateral dimension of the spot voxel increased from ≈150 nm to ≈400 nm as the z-position increased from 2.6 to 3.2 μm above the auto-focused interface between solution and cover slip but saturates thereafter upon further increase. On the other hand, the axial dimension of the spot voxel increased from ≈150 nm to ≈1.4 μm continuously, as the z-position increased from 2.6 to 4.4 μm above the interface without saturation. The AR of spot voxel also increased from <1 to ≈3 continuously as the z-position increased. Linear regression analysis showed that all dimensions significantly associate with z-position ($p < 0.001$ for all). The linear fitting is excellent for height and AR with coefficients of determination (R^2) of 0.948 and 0.944, respectively, but is moderate for width with a R^2 of 0.517. Upon further increase in z-position, a complete single spot voxel toppled down on the substrate–solution interface due to insufficient adhesion. The morphology and dimensions of such complete single spot voxels can therefore be delineated. The single spot voxel takes a shape of ellipsoid and measures 468 nm in width and 1.45 μm in height.

2.4. Voxel Study of Protein Micropillars with Multiple Voxel Layers

The native morphology of single spot voxel is difficult to control as it usually takes the shape of the optical focal volume, an ellipsoid. The ellipsoid is derived from the illumination point

© 2013 WILEY-VCH Verlag GmbH & Co. KGaA, Weinheim

spread function, which is the intensity profile around the focus during two-photon excitation.[11] However, in fabricating 3D continuous structures with pre-defined voxel morphology, one cannot simply fabricate the structures in a spot-by-spot manner because firstly, there is insufficient adhesion between successive ellipsoid spot voxels, and secondly, the fabrication resolution of the continuous structure is limited by the dimensions of the single voxel. In this protein micropillar study, by freely defining the basal voxel morphology through region-of-interest (ROI), square and circle for examples, 3D continuous micropillars taking the shape of square prisms and cylinders were fabricated, respectively, by stacking voxels layer-by-layer via *z*-stack scanning mode. Apart from the key processing parameters investigated so far, a key controlling parameter in fabricating continuous structure is the step size, which defines the distance between the foci of two consecutive laser scanning planes. The morphology of the micropillars and the lateral and axial dimension of the unit voxel layer were investigated to understand the controllability of the fabrication process. The relationship between the input step size and the real height of the layered voxels was also investigated to discover the scaling index of the *z*-stack fabrication. **Figure 4**A,B show the protein square prisms (Figure 4A) and cylinders (Figure 4B) fabricated by *z*-stack scanning at ascending step size from 0.1 to 2.0 µm, with all other parameters fixed. At a small step size of 0.1 µm, burning was observed, probably due to extensive overlapping between layers and hence accumulation of heat. When the step size increased from 0.2 to 0.6 µm, truly smooth and continuous square prisms and cylinders, without obvious laminated structures were fabricated. From a step size of 0.7 to 1.6 µm, laminated structures with increasing height of voxel layers were observed. Starting from a step size of 1.7 µm, delamination of layered voxels was observed in both square prisms and cylinders. The upper layers were completely lost and only the first voxel layer remained on the cover slip, in square prism at a step size of 1.9 µm and in cylinders at 1.8 µm, due to insufficient adherence between layered voxels. The real height of the individual layers was found increasing with ascending step size in a linear manner in both square prisms and cylinders (Figure 4C,D). Linear regression analyses show statistically significant linear regression coefficients of 0.974 and 0.970 ($p < 0.001$) for both square prisms and cylinders with coefficients of determination (R^2_{linear}) of 0.949 and 0.941, respectively, suggesting excellent fitting. The scaling index, defined as the ratio of the real voxel height to the step size in the micropillars was 0.494 ± 0.014 (mean ± standard error of mean) for square prisms and 0.496 ± 0.013 for cylinders, suggesting that the ROI does not affect voxel dimension at all.

2.5. Porosity Study of Protein Matrices

Porosity represents an important property of materials for biomedical applications because it affects cell adhesion, migration, and invasion, as well as diffusion of nutrients and bioactive molecules such as growth factors. Moreover, porosity also affects the mechanical property of the material, which in turn affects the cellular fate processes including adhesion, migration, proliferation, and differentiation. The ultimate goal of controlling the porosity of protein structures using multiphoton photochemical crosslinking is to engineer the controlled drug release properties and mechanical properties of protein microstructures and micropatterns such that user-defined microenvironment or niche can be created to study stem cell fate. In this work, we investigated the controllability of porosity. Methods such as gravimetry[32] and mercury intrusion porosimetry[34] can be used to analyze material porosity but drawbacks such as being inappropriate for sub-micrometer structures and being destructive to samples exist. Image analysis of SEM images is a simple and quantitative method to measure the porosity and pore size for micro- or sub-micrometer structures. In order to investigate the controlling parameters of protein porosity in dual-photon photochemical crosslinking, large, rectangular (29.1 µm × 22.7 µm), and thin protein matrices were fabricated using frame scan mode, such that a large number of images can be sampled from the same matrix for reliable image analysis. **Figure 5**A,B show the laser power dependence of porosity. At 39 mW, no obvious protein matrix but tiny discrete protein particles resulted. From 50 to 80 mW, solid porous protein matrices were successfully fabricated (Figure 5A), suggesting that around 50 mW is a critical threshold for porous matrix formation. At 80 mW, burning at the edges and membrane-like structures were obtained (data not shown), suggesting destructive changes of protein matrices at high laser power because of heat accumulation. Porosity analysis of protein matrices showed inverse relationship between laser power and porosity ranging from 30 to 50% (Figure 5B). When power increased from 50 to 60 and then 70 mW, protein matrix porosity decreased from 47.4 to 35 and then 31.5% and leveled off thereafter. This reduction in porosity can be explained by the fact that higher power means larger amount of photons are delivered per unit time and volume, resulting in higher density of reactive oxygen species available for photochemical crosslinking within the same focal volume and hence higher density, which means number per unit volume, of protein aggregates formed. Regression analysis showed that although the protein matrix porosity significantly and inversely associate with the laser power in a linear manner ($p < 0.001$), an even better fit with a R^2 of 0.991 was found in nonlinear regression. Figure 5C,D shows the exposure time dependence of protein matrix porosity, controlled through number of scanning cycles. At 50 scanning cycles, only loose protein particles but not interconnected protein matrices were deposited (data not shown). Increasing the number of scanning cycles from 100 to 150, 200, and then 250, is equivalent to increasing the exposure time from 1.024 to 1.536, 2.048, and then 2.56 s. At the same power, which means same amount of photons per unit volume and per unit time, the total amount of energy, and hence photons, increased as the scanning cycles or total exposure time increased, resulting in an increase in the sizes of protein aggregates and porosity (Figure 5C). Figure 5D shows that the exposure time, controlled by number of scanning cycles, significantly, linearly, and positively associates with the protein matrix porosity ranging from 40 to 60% porosity ($p < 0.001$) with a low yet significant R^2 of 0.165. Similar to the protein spot study, scanning speed is a co-variant of exposure time. Increasing the scanning speed would result simultaneously in a decrease in exposure time. As a result, the real scanning speed dependence

© 2013 WILEY-VCH Verlag GmbH & Co. KGaA, Weinheim

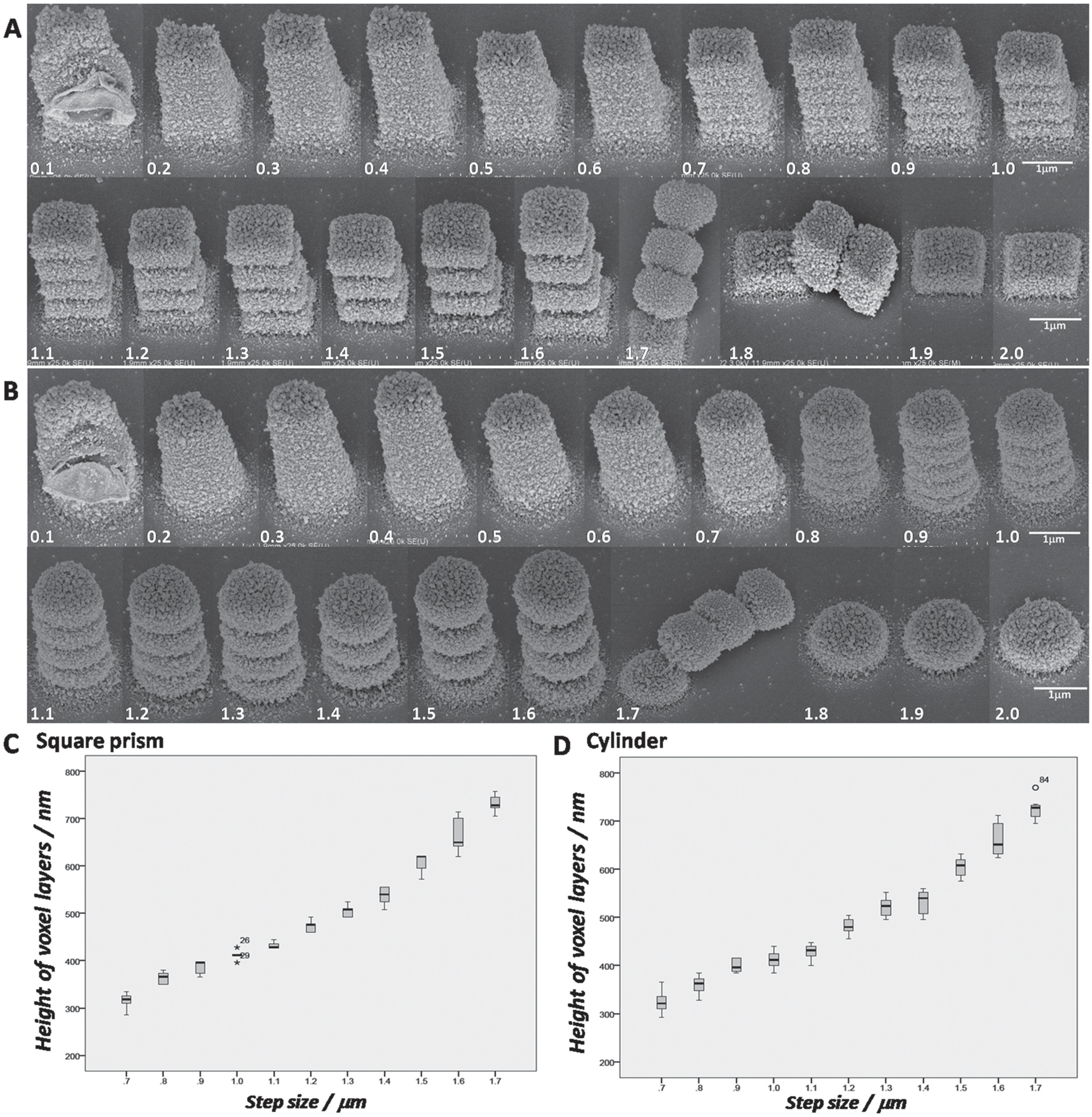

Figure 4. Step size dependence of morphology and dimensions of 3D protein micropillars. Arrays of square prisms and cylinders were fabricated by *z*-stack scan with ROI of square and circle respectively. Step size was increased from 0.1 to 2.0 μm. A,B) SEM images (magnification: 50 KX, scale bar: 1 μm) for A) square prisms and B) cylinders. C,D) Box plot displaying the relationship between the real height of voxel layers and the step size in C) square prisms and D) cylinders ($n = 5$ for both (C,D)).

can only be investigated when the number of scanning cycles is adjusted to keep the exposure time constant. Figure 5E,F show the real effect of scanning speed, represented by pixel dwell time, on protein matrix porosity. There is no obvious change in the size and amount of protein aggregates in the matrix as the scanning speed decreased, corresponding to an increasing pixel dwell time (Figure 5E). Figure 5F shows that the average porosity for all images was around 30%, demonstrating that scanning speed is just an alternative to the number of scanning cycles to vary total exposure time that itself has no effect on porosity when total exposure time is fixed. No significant association was detected between porosity and scanning speed ($p > 0.05$). Figure 5G,H shows the BSA and RB concentration dependence of protein matrix porosity. A threshold RB concentration above 0.2% was identified as no solid matrix structure was fabricated. With increasing concentrations of BSA and RB,

© 2013 WILEY-VCH Verlag GmbH & Co. KGaA, Weinheim

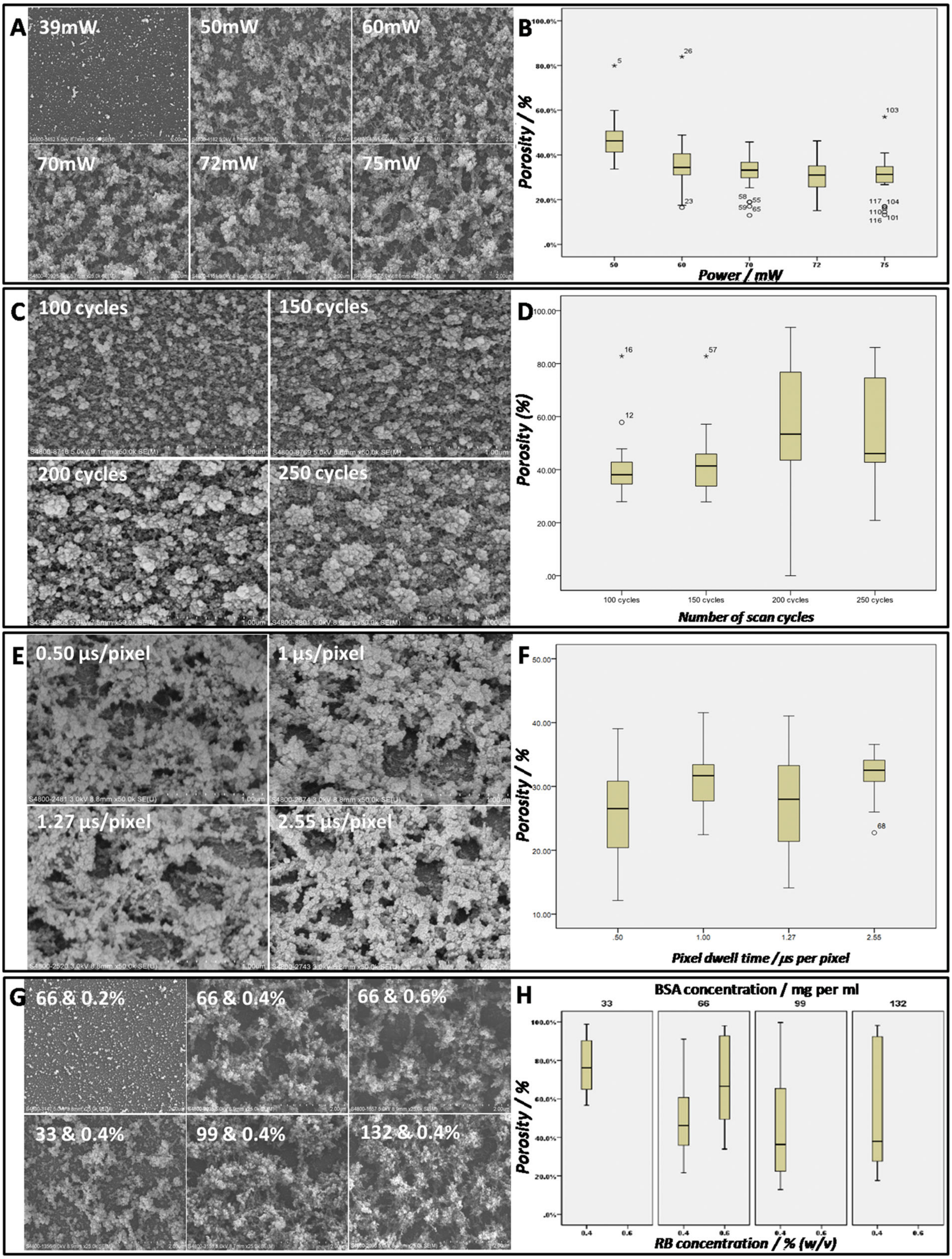

Figure 5. Porosity analysis of protein matrices. A,C,E,G) High magnification SEM images (scale bar: 2 µm for (A,G) and 1 µm for (C,E)). B,D,F,H) Box plots displaying the relationship between protein matrix porosity and different levels of the controlling parameters. A,B) Power dependence ($n = 19$–25). C,D) Exposure time dependence controlled by number of scanning cycles ($n = 30$). E,F) Scanning speed dependence ($n = 18$). G,H) Concentration dependence of BSA and RB ($n = 18$).

© 2013 WILEY-VCH Verlag GmbH & Co. KGaA, Weinheim

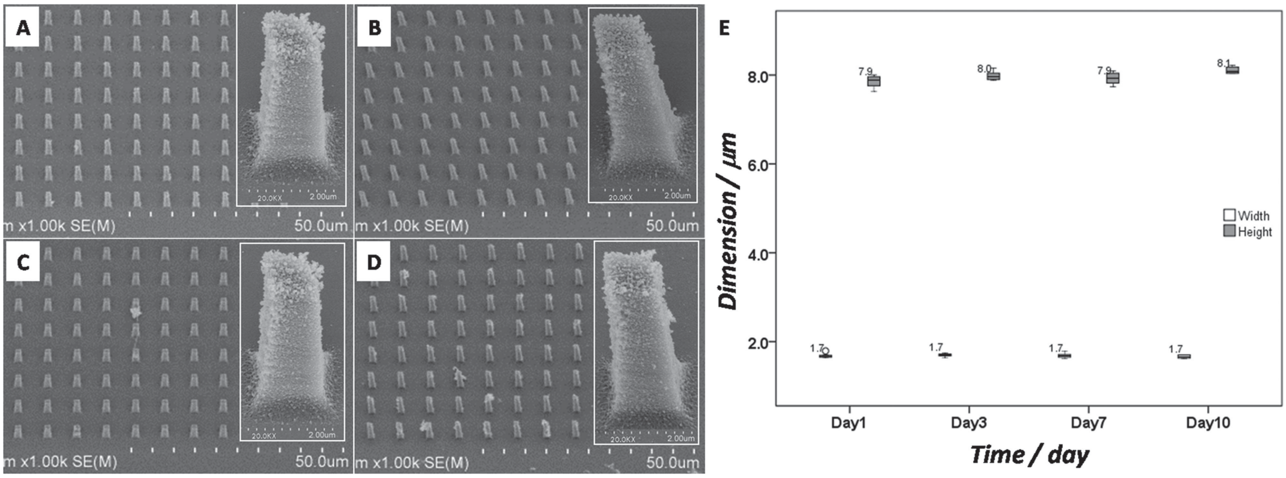

Figure 6. Stability of protein micropillar arrays under cell culture conditions. A–D) SEM images showing the protein micropillar arrays under culture conditions after 1, 3, 7, and 10 days, respectively (scale bar: 50 µm, magnification: 1 KX). Inserts show individual protein micropillar with scale bar of 2 µm and magnification of 20 KX. E) Box plot showing the change in dimensions of micropillar arrays in culture conditions ($n = 10$).

porous matrices with increasing amount of protein available for crosslinking and increasing amount of photo products such as reactive oxygen species were obtained, respectively, leading to increasing amount of protein aggregates, which occupies more volume in the protein matrix, that is, lower porosity. Figure 5H shows an inverse relationship between porosity and BSA concentration. At a fixed RB concentration at 0.4 w/v%, the porosity of protein matrices decreased from 77 to 50% when the BSA concentration increased from 33 to 66 and leveled off thereafter. Regression analysis showed a significant, linear, and inverse relationship between protein matrix porosity and BSA concentration ($p < 0.001$) with a R^2_{linear} of 0.110 while nonlinear regression is also significant ($p < 0.001$), and shows an even better fitting with a $R^2_{\text{quadratic}}$ of 0.199.

2.6. Biodegradation, Cytocompatibility, and Cell–Matrix Interactions

The stability of protein-based micropatterns under culture conditions is very important in applying this platform technology in cell niche studies. **Figure 6** shows the changes in dimensions of protein micropillar arrays under cell culture conditions with culture medium, serum, and other supplements at 37 °C. Figure 6A–D showed that the morphology of protein micropillars was not changed over time. Figure 6E is the box plot of protein micropillar dimensions. Both the height and the width of the protein micropillars showed no notable degradation over time. One-way analysis-of-variance (ANOVA) showed no difference at all ($p = 0.330$) in micropillar width. As for micropillar height, although there is statistical significant difference between day 1 and day 10 according to Dunnett T3 poat-hoc test ($p < 0.001$), the actual difference for a 8 µm micropillar was only 0.25 µm, which might be attributable to measurement errors or slight swelling over time. Such difference is practically insignificant, suggesting that protein micropillar arrays exhibited good stability under culture conditions. Another important criterion of being micropatterned substrates for cell niche studies is the cell compatibility including cell attachment, survival, and exhibition of physiological functions such as extracellular matrix deposition. **Figure 7** shows fibroblasts culture in BSA micropillar arrays within protein microwells without any matrix coating. RB was red fluorescent, and therefore used to visualize the micropillar arrays and the microwell immediately after fabrication (Figure 7A). Figure 7B shows green fluorescent quantum dots labeled fibroblasts cultured on micropillar arrays immediately after seeding. Cells were randomly distributed and still relatively round and less spread. Figure 7C shows the live and dead staining of fibroblasts after 7 days of culture on the micropillar arrays. Cells were all alive and well spread that they covered almost all spaces within the microwell. Figure 7D shows the SEM image of fibroblasts on micropillars after 1 day of culture from the top view. Figure 7E–H shows the SEM images with 30 degrees of rotation of selected fibroblasts on micropillar arrays. Fibroblasts cultured on micropillar arrays were more 3D-like that the contours of the cells and their membranes can be observed, than those cultured as 2D monolayers on cover slips where cells were super flattened (Figure 7L). Fibroblasts were not only attaching to the protein micropillars but also pulling individual micropillars and bending them (Figure 7G–K). Apart from wrapping around the micropillars with adhesion-like structures (Figure 7K), fibroblasts also gripped on the waist of micropillars (Figure 7J), suggesting that fibroblasts were able to detect the full depth of the protein micropillars. Expression of matrix adhesion molecules is necessary for subsequent cellular activities including proliferation, migration, and differentiation, and is therefore an important indicator for cytocompatibility of a material. **Figure 8** shows the immunofluorescent staining of cell-matrix adhesion molecules in fibroblasts on day 1 of culture on either the 3D protein micropillar array or 2D glass cover slip. When cultured on the protein micropillar arrays, fibroblasts were able to express integrin α_v, a transmembrane matrix receptor and a marker for focal

© 2013 WILEY-VCH Verlag GmbH & Co. KGaA, Weinheim

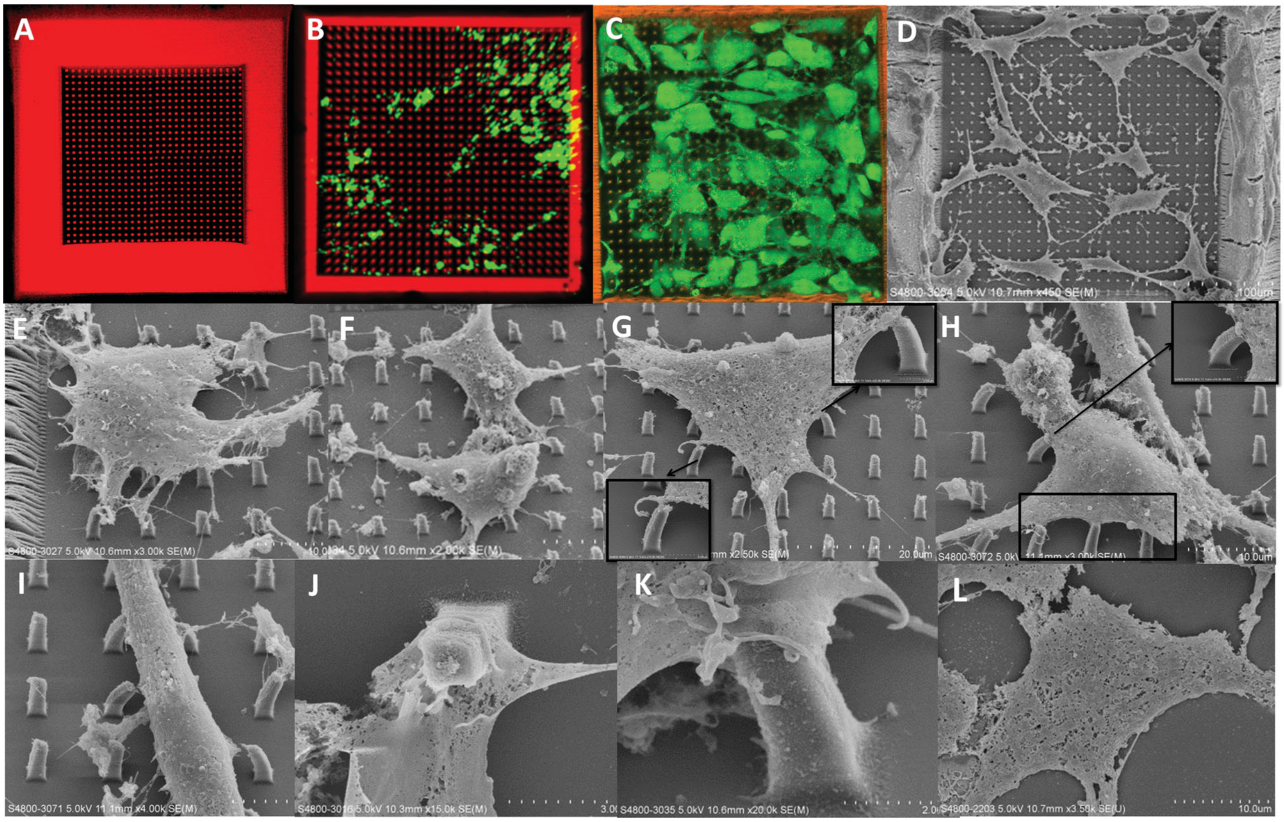

Figure 7. Fibroblasts cultured on protein micropillar arrays. A) Fluorescent image of protein micropillar arrays (red) within a protein microwell (red) immediately after multiphoton photochemical crosslinking-based fabrication. B) Quantum dot labeled 3T3 fibroblasts (green) on protein micropillar arrays (red) within a protein microwell (red) immediately after seeding. C) Live and Dead staining of fibroblasts cultured on protein micropillar arrays within the protein microwell for 7 days. D) SEM image of fibroblasts seeded on protein micropillar arrays within protein microwell on day 1 post-seeding (scale bar: 100 µm). E–K) SEM images showing the morphology of fibroblasts cultured on protein micropillar arrays. E) A fibroblast growing on micropillars close to the microwell. F) Two fibroblasts on micropillars touching each other (scale bar: 10 µm). G,H) Fibroblasts spreading on micropillars by pulling on and bending individual micropillars (scale bars: 20 µm for (G) and 10 µm for (H)). Magnified views of bending individual micropillars are shown as inserts. I) Extending part of a fibroblast pulling on and bending the individual micropillars (scale bar: 10 µm). J) Edge of a fibroblast gripped on the waist of a micropillar (scale bar: 3 µm). K) Edge of a fibroblast was bending a single micropillar with adhesion-like structures wrapping around the micropillar tip (scale bar: 2 µm). L) SEM image of highly spread and flattened fibroblasts cultured as 2D monolayers on cover slip (scale bar: 10 µm).

adhesions, in a dot-like morphology (Figure 8A,B), which suggests formation of stable adhesion structures. The expression of integrin β1, a less specific matrix receptor, in fibroblasts on micropillars was also positive but less frequent than integrin α_v (Figure 8C,D). Paxillin, an intracellular marker for and also important component of focal adhesions, was highly positive and largely dot-like in fibroblasts cultured on micropillar arays (Figure 8E,F). Comparing with fibroblasts cultured on micropillar arrays, cells also express abundantly integrin α_v (Figure 8G,H) and less frequently integrin β1 (Figure 8I,J) in dot-like manner on 2D when cultured on glass cover slip. However, on cover slip cultures, fibroblasts express more abundant paxillin intracellularly in a less dot-like manner (Figure 8K,L) than those cultured on micropillar arrays (Figure 8E,F), suggesting that the pxillin-containing adhesion structures are more stable in the micropillar array cultures. Figure 8 showed that fibroblasts attach to and form stable adhesions on BSA protein micropillar arrays without any matrix coating, suggesting excellent cytocompatibility of the BSA protein micropillar arrays. A third criterion for excellent cytocompatibility in functional biomaterial is the ability of the material to support physiological functions of cells such as synthesis, secretion, and deposition of extracellular matrix. **Figure 9** showed the extracellular matrix components deposited by fibroblasts cultured on protein microspillars and glass cover slips. After 7 days of culture, fibroblasts were able to synthesize and deposit fibronectin fiber meshwork on both micropillar arrays (Figure 9A,B) and glass cover slip (Figure 9G,H) while the latter seems to be more extensive. Vitronectin, an extracellular matrix component known to bind to integrin α_v-based adhesion structures, was found highly positive in fibroblasts cultured on both protein micropillars (Figure 9C,D) and glass cover slip (Figure 9I,J), while the latter seems to be more abundant. This result matches well with the integrin

© 2013 WILEY-VCH Verlag GmbH & Co. KGaA, Weinheim

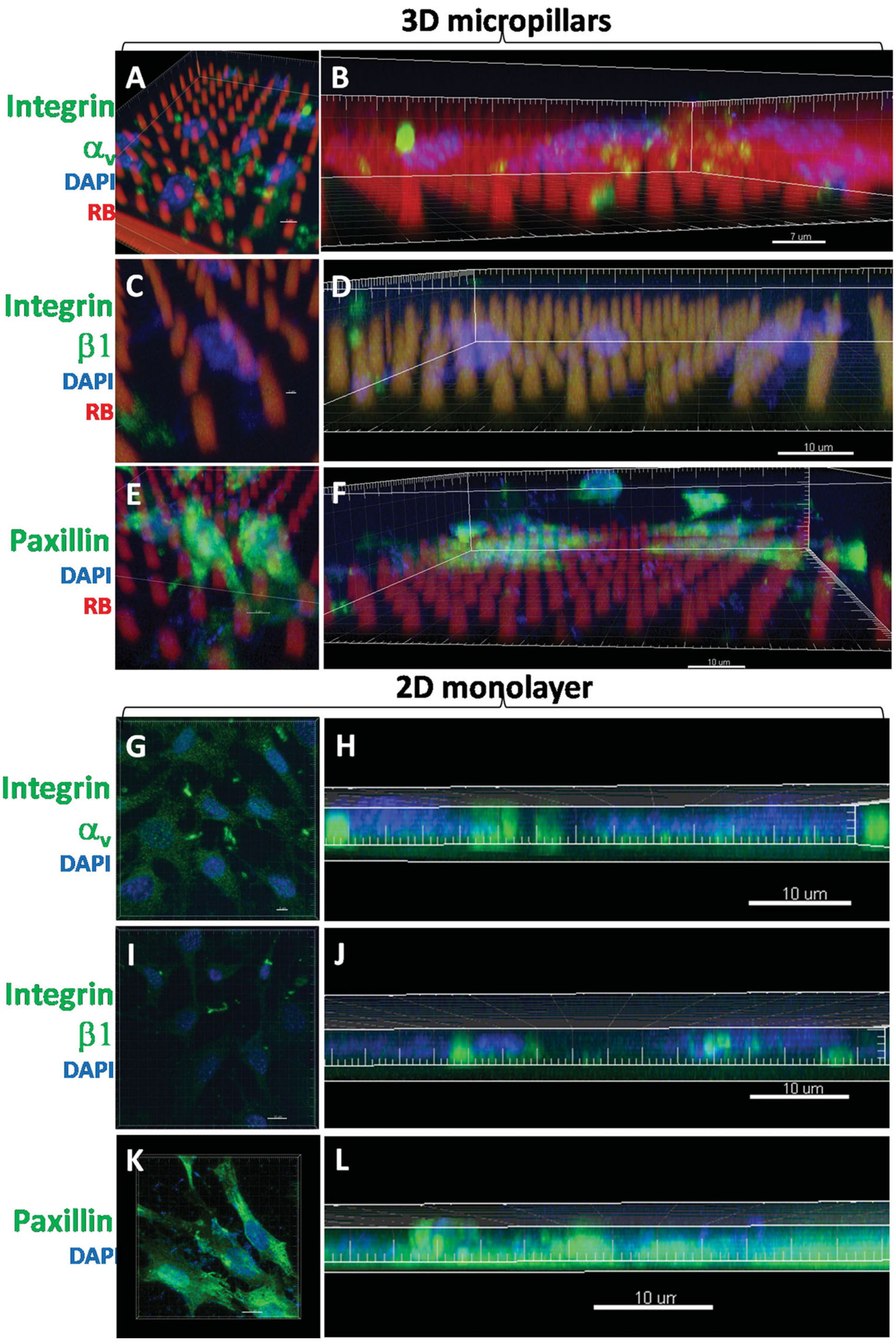

Figure 8. Confocal laser scanning microscopic images showing the immunofluorescent staining of cell-matrix adhesion molecules in fibroblasts cultured on different substrates. Fibroblasts cultured on A–F) 3D protein micropillars and G–L) 2D glass cover slip. Cell matrix adhesion molecules stained include A–B,G–H) Integrin α_v, C–D,I–J) Integrin β1, and E–F,K–L) paxillin. Confocal images showing A,C,E,G,I,K) the top views (with scale bars of 1 µm) and B,D,F,H,J,L) side views (with scale bars of 5 µm for (H,J), 7 µm for (B), and 10 µm for others) of fibroblasts in cultures. Green: cell matrix adhesion molecules; blue: DAPI counterstaining for nuclei; red: Rose Bengal (RB) photosensitizer.

α_v immunopositivity in Figure 8A,B,G,H. Collagen I, an extracellular matrix known to be synthesized by fibroblasts and hence a marker of fibroblasts, was stained positively on both micropillar arrays (Figure 9E,F) and glass cover slip (Figure 9G,H), while the collagen was deposited throughout the full thickness of the micropillars.

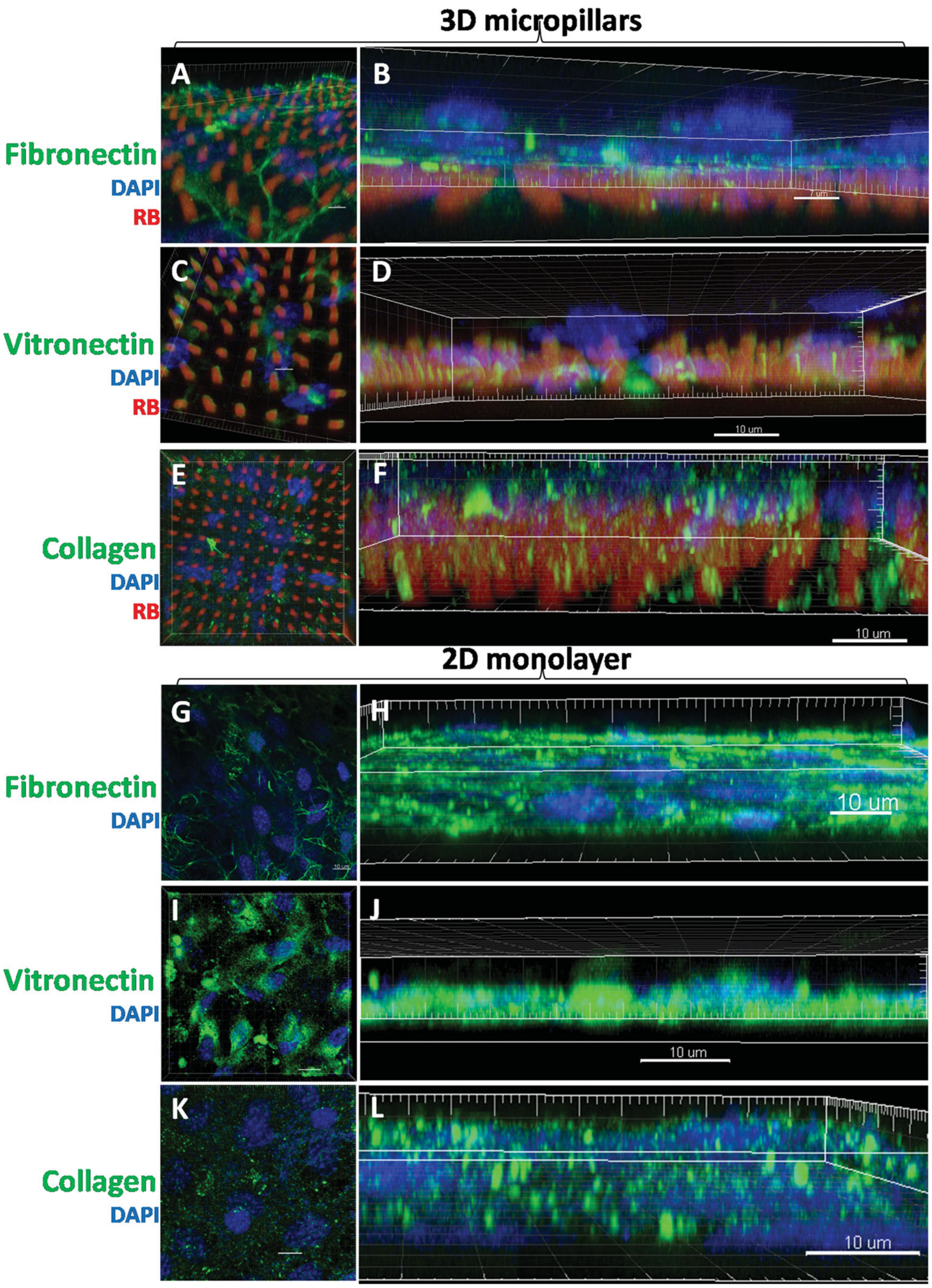

Figure 9. Confocal laser scanning microscopic images showing the immunofluorescent staining of extracellular matrix components deposited by fibroblasts cultured on different substrates. A–F) Fibroblasts cultured on 3D protein micropillars without any coating. G–L) Fibroblasts cultured as 2D monolayer on cover slips without any coating. Extracellular matrix components stained include A–B,G–H) fibronectin, C–D,I–J) vitronectin, and E–F,K–L) paxillin. Confocal images showing A,C,E,G,I,K) the top views (with scale bars of 1 µm for (A,C,E), with scale bars of 10 µm for (G,I,K)) and B,D,F,H,J,L) side views (with scale bar of 7 µm for (B) and 10 µm for others) of fibroblasts in cultures. Green: extracellular matrix components; blue: DAPI counterstaining for nuclei; red: RB photosensitizer.

3. Discussion

3.1. Optical Resolution Versus Fabrication Resolution

The optical resolution of multiphoton microscopy can be defined as the square of the illumination point spread function (IPSF2), which describes the intensity in space near the focus.[11,35] Theoretically, the focal volume can be represented and calculated by a Gaussian approximation where full-width half maximum (FWHM) is a more common measure of optical resolution, and used to characterize the dimensions of the 3D Point spread function.[36] By fitting the parameters used in

© 2013 WILEY-VCH Verlag GmbH & Co. KGaA, Weinheim

the current work to the following functions, a wavelength of 800 nm, an oil lens with N.A. of 1.3 and a refractive index (*n*) of 1.56 for the immersion oil, the diffraction-limited lateral (ω_{xy}), and axial (ω_z) 1/e radii of IPSF2, and hence the FWHM at both lateral and axial directions were calculated as follows:

$$\omega_{xy} = 0.325\lambda / \left(\sqrt{2}\mathrm{NA}^{0.91}\right) \quad \text{for NA} > 0.7 \qquad (1)^{[11]}$$

$$\omega_z = \left(0.532\lambda/\sqrt{2}\right)\left[1/\left(\mathrm{n} - \sqrt{\left(\mathrm{n}^2 - \mathrm{NA}^2\right)}\right)\right] \qquad (2)^{[11]}$$

where ω is the distance where the intensity (I) is 37% of its maximum value.

$$\mathrm{FWHM}_{xy} = 2\omega_{xy}\sqrt{\mathrm{In}2} \qquad (3)^{[34]}$$

$$\mathrm{FWHM}_z = 2\omega_z\sqrt{\mathrm{In}2} \qquad (4)^{[34]}$$

Therefore, the calculated FWHM_{xy} (lateral optical resolution) is 241 nm and the FWHM_z (axial optical resolution) is 718 nm.

In multiphoton-based fabrication, the optical resolution, theoretically calculated, is different from the fabrication resolution, which depends on many interacting processing parameters. In other words, the optical voxel, which basically means the focal volume of the laser spot, is different from the fabrication voxel, which defines the primitive structural element during fabrication. As a result, understanding the factors controlling the fabrication voxel is very important for rational design and accurate fabrication of 3D structures. In this work, by using different modes of scanning, we have fabricated line, spot, and micropillar voxels to study their morphology and dimensions, delineate the lateral and axial fabrication resolution, and to demonstrate the controllability of key parameters on voxel morphology and dimensions. The fabrication voxel is related to the dimension of the optical voxel, which defines the theoretical volume with effective multiphoton excitation[11] and therefore crosslinking. However, many other factors affect the actual size of the fabrication voxel. First, the probability of multiphoton excitation saturates near the focal center but can continue to increase in the wings of the focal volume, particularly with a fluorophore of high two-photon cross-section, leading to effective excitation volume larger than the theoretical focal volume.[37] Second, shrinkage upon post-fabrication processing including graded ethanol dehydration and critical point drying may reduce the size of the fabrication voxel. Third, the mechanism of voxel formation matters. During the initial exposure time, the voxel formed usually takes the shape determined by the point spread function (PSF) relatively to the threshold light intensity, and is therefore close to the theoretical optical voxel. This mechanism is regarded as “focal spot duplication”.[13] However, as the exposure time increased, “voxel growth” becomes the dominating voxel formation mechanism,[13] which is caused mainly by diffusion of photoproducts such as free radicals,[13] but other mechanisms such as waiveguiding by voxels and beam distortion by the polymerized portion[33] and scattering effects[38] are also important. This exposure-time-dependent mechanism shift of voxel formation was supported by the phenomenon that the dimension of the voxel increases rapidly with power but then decreases and saturates with time.[13] In the current study, the mechanism shift has also been demonstrated in the protein line and the protein spot experiments. Moreover, in the spot and micropillar studies, saturation of voxel width but not height suggests the wave guiding effect along the long axis of the fabricated portion of the voxel exists. Fourth, power directly affects the PSF dimensions and positively associates with the voxel dimension as demonstrated in the line, sport, and micropillar voxel studies. Fifth, photosensitizer and acceptor concentrations also affected the voxel dimension as demonstrated in epoxy resins[39] and proteins in the current study.

3.2. Ascending *z*-Stack Scan is a New and Better Method for Voxel and Fabrication Resolution Study

In order to investigate the voxel morphology and dimension, two methods, namely, ascending line scan and ascending spot scan, have been used.[12,13] Small lateral resolution such as protein lines of ≈600 nm in width[24] and polymer particle of 120 nm in diameter[40] has been demonstrated using multiphoton fabrication. In the current study, we also demonstrate small lateral fabrication resolution by fabricating protein lines of 200 nm width and protein spots of 400 nm diameter. In defining the axial fabrication resolution of epoxy resin, the ascending spot scan method with various starting *z*-positions has identified that the complete epoxy resin voxel toppled down on the substratum took a spinning ellipsoid shape with lateral and axial dimensions of 1.4 and 3.4 µm, respectively, equivalent to an AR of 2.4.[12] In the current study, protein spot voxels taking the same ellipsoidal shape can be much smaller than the polymer-based voxels, with a lateral and axial fabrication resolution of 0.468 and 1.45 µm, respectively. More importantly, this work reports a new and better method, namely ascending *z*-stack scan, which can be used not only for determining voxel morphology and dimension, but also for verifying theoretical optical resolution and further down-tuning the axial fabrication resolution below the theoretical value. In the current study, voxel layers down to 350 nm of axial fabrication resolution, smaller than the theoretical axial optical resolution (718 nm), can be fabricated with excellent controllability of voxel dimensions. This ascending *z*-stack method conducted multiple successive scanning cycles in the *z*-direction to fabricate 3D structures with repeated voxel layers at increasing step size from 0.1 to 2.0 µm. When the step size is below 0.7 µm, the distance between any two consecutive foci was below the theoretical axial optical resolution, 718 nm in this study. Effectively, the overlap between successive focal volumes was so extensive that individual voxel layers cannot be resolved, resulting in fabrication of truly smooth and continuous structures. Starting from 0.7 µm, laminated voxel layers were observed, in both square prisms and cylinders. At this point, the intensity peaks between two consecutive optical foci can be resolved, therefore leading to the resolution of voxel layers. Increasing the step size from 0.7 to 1.6 µm leads to a linear increase of the axial dimension of repeating voxel layers, from 350 to 800 nm. This is equivalent to a fabrication scaling index of 0.5, referring to

© 2013 WILEY-VCH Verlag GmbH & Co. KGaA, Weinheim

a 50% tune-down of the axial fabrication resolution. The less-than-unity fabrication scaling index of the z-stack method is owing to the overlap between porous fabrication voxels that the gravity-driven sedimentation of crosslinked protein aggregates from the current z-position to the lower layers through the porous structures and the post-fabrication processing-induced shrinkage. Excellent controllability over voxel dimension is found within a working window between a step size of 0.7 μm, from which the intensity peaks between consecutive optical voxels starts to be resolved, to a step size of 1.6 μm, above which the fabrication voxels no longer overlap. When the step size is above 1.6 μm, there is minimal overlap between successful voxel layers and therefore insufficient adhesion between consecutive voxel layers, leading to de-lamination of upper voxel layers, as shown in both the square prisms and cylinders. This phenomenon therefore delineates the real axial dimension of voxels to be 1.6–1.7 μm, similar to 1.5 μm as determined in the 3D spot voxel study. All in all, the ascending z-stack method experimentally verified the axial optical resolution at 700 nm, delineated the axial dimension of layered voxels at 1.6–1.7 μm, and pushed the axial fabrication resolution below the optical resolution limit. The advantage of the current ascending z-stack scan method over the ascending spot scan method is that it determines the axial dimension of voxels with reproducibility in multiple voxel layers of the z-stacked structures, and thus provides an averaged and more accurate estimate of the real axial dimension of single voxels. Another major advantage of this method is that the thickness of the repeating voxel layers, that is, the axial fabrication resolution, can be pushed below the theoretical optical resolution limit, a feature that has not been achieved in any other photopolymerization platforms. We therefore concluded that the axial fabrication resolution is not necessarily limited by the theoretically calculated optical resolution, but controllable by the step size of the ascending z-stack method.

3.3. Advantages of Protein Micropillar Array Based Cell Culture System

Similarly to other microfabricated patterns using polymers, there is minimal degradation over culture time in the protein micropillar arrays because the structures were covalently crosslinked so that they are stable enough to resist degradation under culture conditions. Most microfabrication technologies utilized PDMS-based lithography platforms, which requires complicated procedures including PDMS molding, silanization, substrate mounting, fluorescent labeling of the microposts, and extracellular matrix coating such as fibronectin[41,42] and laminin[43] via microcontact printing, and generates problems including prolonged PDMS curing and collapsed microposts.[41,42,44,45] While the current protein based free-writing microfabrication platform is a simply "write-and-seed" procedure and eliminates all lengthy processing steps, dramatically reducing the time to prepare for cell culture experiments. Specifically, no molding procedure is required, the photosensitizing dye used for multiphoton photochemical crosslinking is intrinsically fluorescent, eliminating the labeling procedure, and the protein nature makes the micropillar arrays cytocompatible that cells can bind to the micropillar array with cell matrix adhesion molecules without the need to coat any other matrix proteins. The elastomer method using PDMS technology uses at least 2 days of preparation before cell culture while in the current protein micropillar array method, only less than four minutes were required for fabrication before cell seeding. Binding of fibroblasts to BSA micropillar arrays are similar to those in native matrix as cell matrix adhesion proteins including integrin alpha α_v and $\beta 1$, and paxillin were expressed. Another characteristic of the protein micropillar array is that cells appear more 3D-like than those of 2D monolayer cultured cells, reflected by a more "3D-like" morphology. Furthermore, fibroblasts were able to deposit extracellular matrix such as type I collagen and fibronectin on the protein pillars such that a more physiologically relevant binding and microenvironment can be created using this micropillar platform. Finally, the micropillar arrays have mechanical properties matching well with the matrix mechanical properties such that cell can bend the micropillars as they apply traction force while migrating.

3.4. Potential Biomedical Applications of Multiphoton Photochemical Crosslinking Based Fabrication

Using multiphoton excitation, simple structures such as lines[20] and patterns[46] can be used for biomedical applications such as neuronal cells guidance. The current work demonstrates the capability to fabricate a wide spectrum of protein structures and patterns with sub-micrometer features and excellent controllability in voxel dimension, morphology and porosity, using femto-second laser-based multiphoton photochemical crosslinking. This platform has the potential to provide a better alternative to existing PDMS or other polymer-based sub-micrometer fabrication systems due to the biocompatible, cytocompatible, porous and bio-mimetic nature of protein materials. First, protein structures and patterns with controllable properties including user-defined topological features, porosity and associated drug release rates and mechanical properties can be fabricated and used directly for cell culture. This platform enables studies of interactions between cells and their niche factors including matrix, soluble factor, mechanical ones without any coating procedure, demonstrating simplicity of this platform. For example, structures and patterns with gradient porosity such as the protein matrix with ascending porosity can be fabricated to aid gradient drug release patterns. A previous study has reported that, by controlling the laser power and exposure time, the dye diffusion properties of protein structures were obtained.[47] We speculated that the change in diffusion properties might result from different microstructures and porosity in the protein structures crosslinked at different power, as demonstrated by the current study. Another example is that micropatterns with gradient mechanical properties can be fabricated by controlling various parameters, including those controlling porosity. In our ongoing study on mechanical properties of the protein micropillar arrays, a reduced elastic modulus of around 40 KPa has been measured under a standard fabrication condition, using atomic force microscopy nanoindentation (data

© 2013 WILEY-VCH Verlag GmbH & Co. KGaA, Weinheim

not shown). Controllability over the mechanical properties of protein micropillars would enable further applications of this platform in studying the mechanical niche of cells and using a traction force sensor as that have been demonstrated with elastomer microposts.[44,45] Second, multiple extracellular matrix components such as fibronectin, laminin, and collagen can be included during the crosslinking fabrication process so as to further functionalize the BSA microstructures and micropatterns with bioactive signals, and thus engineer complex cellular niches or microenvironments. By specifying the matrix components of the microstructures, we may be able to control the cell-matrix adhesions of different types and maturity such as focal adhesions and fibrillar adhesions[48] so as to exert control over the extent of cell-matrix interactions and hence the cell fate. Third, arrays of micropillars with different lateral and axial dimensions and morphologies can be fabricated to create 3D topological microenvironment. Topological features have been demonstrated to affect cell activities including proliferation, alignment, and differentiation.[43] As shown in the current study, cells appear more 3D in micropillar arrays than 2D monolayer cultures, this platform may have the potential to create pseudo- or real-3D microenvironment, mimicking that of native microenvironment. Together with other controllable properties such as soluble signal release rate, matrix components, and mechanical properties, this platform has the potential to engineer a real user-defined 3D cell niche.

4. Conclusions

This work demonstrated free writing fabrication of a wide range of user-defined 3D protein microstructures and micropatterns with sub-micrometer features using dual-photon photochemical crosslinking. The protein voxel morphology and dimension have been studied in detail for the first time and a new method determining optical and fabrication resolutions and exerting excellent controllability over voxel morphology and dimension namely ascending *z*-stack scan has been proposed. A lateral fabrication resolution of 200 nm has been demonstrated from the line voxel study. Single 3D spot voxel is ellipsoid-shaped with a 400 nm lateral and a 1.5 μm axial resolution. In fabricating continuous 3D structures, the morphology and the axial fabrication resolution of layered voxels can be controlled by the step size during *z*-stack scan. Truly continuous and smooth structures without any layered voxel structures can be fabricated at low step size while the layered voxels with lateral and axial fabrication resolution of 350 nm can be fabricated. The real axial dimension of voxel layers determined in the current study is 1.6 μm. The ROI determines the micropillar morphology, circular for cylinder and square for square prism, respectively. The step size linearly controls the dimension of the layered voxels with a scaling index of 0.5. Furthermore, both the voxel dimension and the porosity of protein structures are controllable by laser power and exposure time, *z*-position for fabrication, and BSA and RB concentrations but not scanning speed. Finally, protein micropillar array presents a simple “write-and-seed” cell culture system, the micropillars exhibited good stability under culture conditions and excellent cytocompatibility that fibroblasts attach, express matrix adhesion molecules and deposit extracellular matrix components on the micropillars without the need to coat any matrix. This work lays down solid foundations to engineering user-defined complex protein matrix with micrometer to sub-micrometer features for future biomedical applications such as cell niche studies.

5. Experimental Section

Dual-Photon Confocal Laser Scanning Microscopy (CLSM): Multiphoton photochemical crosslinking-based biofabrication of protein structures works well in all three multiphoton laser scanning microscopy systems (Carl-Zeiss 510 (Z-510), Carl-Zeiss 710 (Z-710), and Leica SP5 (L-SP5)) used, and all were equipped with mode-locked Ti:Sapphire femtosecond near infrared (NIR) laser (Coherent, Santa Clara, California, USA) with peak output at the wavelength of 800 nm. Data shown here are those fabricated by the Carl-Zeiss 710, with a 40× oil lens (N.A. = 1.3) and at a wavelength of 800 nm. The actual output laser power was measured immediately after the objective using a power meter (Coherent) every time before fabrication. The default software (Zen 2009, Carl Zeiss) was used for controlling different fabrication parameters.

Sample Loading System: A glass slide (76 mm × 26 mm × 1 mm) (Marienfeld, Paul Marienfeld GmbH & Co. KG, Lauda-Königshofen, Germany), a coverslip (18 mm × 18 mm) (Marienfeld, Paul Marienfeld GmbH & Co. KG, Lauda-Königshofen, Germany) and a circular press-to-seal silicone isolator (9 mm in diameter, 1.0 mm in depth) (Invitrogen, Life Technologies Corporation, Oregon, USA), which was used as a spacer to between the glass slide and the coverslip when constructing the sample loading system for fabrication, were used. These components were firstly cleaned in ultrasonic bath in acetone for five minutes, and in isopropanol for another five minutes before immersing in absolute ethanol until use. Immediately before use, the components were thoroughly rinsed in deionized water. The silicon isolator was firstly press-to-seal on the coverslip. An aliquot of the sample protein BSA (Sigma-Aldrich) (50 μL) and the photosensitizer RB (Sigma-Aldrich) solution at appropriate concentrations was loaded into the circular chamber before gently pressing the glass slide against the silicon spacer to form the “sandwiched” sample loading system (**Figure 10**) for subsequent fabrication. The system was mounted on the sample stage of the inverted microscope of the CLSM system with the coverslip side facing the objective.

Defining the Focus Position for Fabrication: The focus position of laser is of great importance because it determines the effective shape and dimension of the focal volume during multiphoton excitation and subsequent fabrication. It also directly affects whether the fabricated structure can be well adhered to the coverslip substrate or floated away. Two methods can be used to define the focus position. The first method was to tune the *z*-position of the objective up and down until the two-photon fluorescence signals of RB in the solution increased dramatically. The second method was to use the autofocusing function in Z-710 in reflection mode or fluorescence mode. If the latter is used, Argon laser 488 instead of NIR laser was used for autofocusing because NIR laser would have started the excitation during autofocusing through the

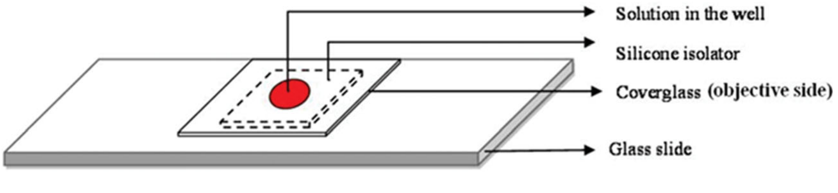

Figure 10. Schematic diagram showing the sample loading system for fabrication.

© 2013 WILEY-VCH Verlag GmbH & Co. KGaA, Weinheim

solution. Therefore, in this work, autofocusing in reflection mode was used.

Fabrication of Protein Lines for Voxel Study: Line with time series scan mode was used to fabricate sub-micrometer protein lines for voxel study particularly with the lateral dimension (width). The scan configuration for fabrication was set as 512 × 1 pixels. The dependence of the width of protein lines on major controlling parameters including power and number of scan cycles was investigated. The parameters were defined in Supporting Information, Section 1. Line scan was performed and structures fabricated were processed for SEM analysis as described above. SEM images at high magnification (25 KX) were used for measurement of line width. Six positions per each line were randomly selected and measured while three lines per each fabrication condition were analyzed.

Fabrication of Protein Spots for Voxel Study: Spot with time series scan mode was used to fabricate protein spots for voxel study for both the lateral and the axial dimension. The dependence of the spot dimension and AR on major controlling parameters including power, number of scan cycle, pixel dwell time, and *z*-position was investigated. Repeated spot scan was performed after autofocusing as described above. Zero *z*-position was used as the reference point and a wide range of *z*-position was screened in order to delineate the real morphology and size of voxel. The parameters were defined in Supporting Information, Section 2.

Fabrication of Protein Micropillars for Voxel Study: *Z*-stack (*xyz*) scan mode, defined as a stack of scanning planes in the *z*-position, was used to fabricate protein micropillars. The cross-section of the micropillar was firstly defined by selecting a ROI in terms of a circle with a diameter of 1.6 µm or a square with 1.6 µm width. An array consisting of a matrix of 4 × 6 such circles or squares was defined in the scanning region prior to fabrication. Step size or interval between scan cycles was the distance between each focal plane. The focus for scanning would move one step size up after one frame scan. The multiple of the number of scan cycles or optical sections and the step size would be the theoretical height of the protein micropillar, which is kept constant in all structures. The parameters for fabrication were defined in Supporting Information, Section 3.

Fabrication of Protein Matrices for Porosity Study: Frame with time series scan mode was used to fabricate large area rectangular protein matrix to assure random and large sampling during the subsequent image analysis-based porosity analysis. The dependence of porosity on major fabrication parameters including laser factors such as power, scanning factors such as pixel dwell time and number of scanning cycles, and substrate factors such as concentrations of BSA and RB was studied. After auto-focusing, a frame scan was conducted with a 512 × 512 pixels resolution at an optical zoom 7.3, representing ≈0.057 µm pixel^{-1}. The parameters used were shown in Supporting Information, Section 4. After scanning, the sample was rinsed with RO water for five times, three minutes for each time. The coverslip with the fabricated protein matrix adhered on was taken back to the sample stage for imaging again with a HeNe laser providing excitation light at wavelength of 543 nm to verify the fabrication of protein matrices, making use of the intrinsic fluorescent property of RB, before processing for subsequent SEM analysis.

Fabrication of Other Protein Structures and the Complex Pier-Bridge Structures: Frame with time series scan mode was used to fabricate freely defined patterns such as the “HKU” letters. *Z*-stack scan mode was used to fabricate other 3D structures such as microwells. For the complex pier-bridge structure, a total of 10 ROIs were designed to define the frames or areas that the laser beam travels at each 2D planes. *Z*-stack mode with fixed power at 45 mW, fastest scanning speed at 0.5 µs pixel^{-1}, was used to fabricate the structure at a defined sequence (**Figure 11**).

SEM Analysis: SEM (Leo 1530 FEG SEM and Hitachi S-4800 FEG SEM) was used to evaluate the protein ultra-structures after fabrication. In brief, samples were firstly rinsed thoroughly in RO water to remove excess RB and BSA. Then they were fixed with glutaraldehyde (Sigma-Aldrich) solution (2.5 w/v%) for 20 min and then gradually dehydrated by rinsing in a series of ethanol solution (25, 50, 70, 80, and 90%) for once and then absolute ethanol for twice, three minutes for each rinse. These samples were further dehydrated by critical point drying (BAL-TEC CPD 030), mounted on metal stab, and sputter coated with gold for 100 s. SEM images at different magnifications were taken for subsequent voxel and porosity analysis. In order to get a 3D view of the micropillars, SEM images were taken with a 30° tilting in the sample stage. The height and diameter of the micropillars were measured from SEM images using the software Image J and correction for the tilted sample stage was done in calculating the real height and aspect ratio (AR).

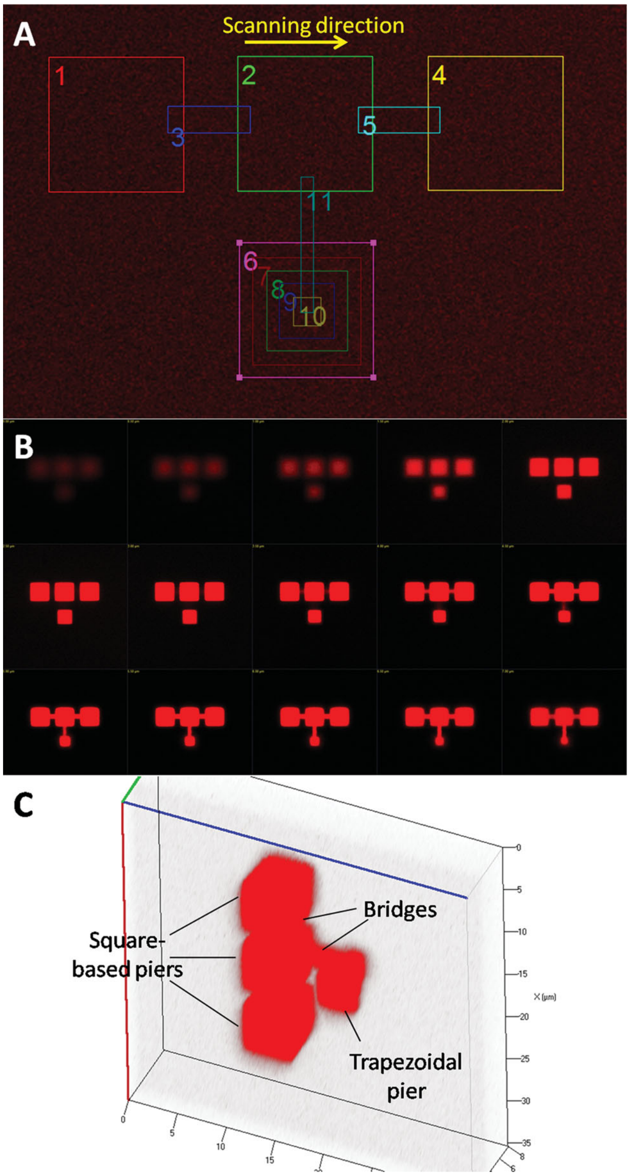

Figure 11. Steps fabricating the complex bridge-pier structure. A) Design of ROIs (1–10). B) Fluorescent images of the structures during fabrication. C) 3D fluorescent image of the complex bridge-pier structure. Scan sequence: 1) Simultaneous scan of ROI (1), (2), and (4) (*z*-stack mode: from –1.0 to 6.5 µm, step size: 1.5 µm, dimension for each ROI: 5 µm × 5 µm). 2) Simultaneous scan of ROI (3,5) (*z*-stack mode: from 5.0 to 6.5 µm, step size: 1.5 µm). 3) Scan of ROI (6–10) (time series mode: 2 cycles; position: 0.0 µm for (6), +1.5 µm for (7), +3.0 µm for (8), +4.5 µm for (9), and +6.0 µm for (10); size: 5 µm × 5 µm for (6), 4 µm × 4 µm for (7), 3 µm × 3 µm for (8), 2 µm × 2 µm for (9), and 1 µm × 1 µm for (10). 4) Scan of ROI (11) (time series mode: 2 cycles; position: +6.0 µm; size: 0.5 µm × 0.5 µm).

© 2013 WILEY-VCH Verlag GmbH & Co. KGaA, Weinheim

Measurement of Protein Matrix Porosity: Porosity of the rectangular matrices fabricated was measured by quantitative processing of SEM images using a professional imaging processing software MetaMorph (Molecular Devices, Downingtown, Pennsylvania, US). Five fields at a magnification of 5 KX or ten fields at a magnification of 50 KX were randomly selected, and imaged for each sample and at least three samples per fabrication condition were analyzed. After auto contrast enhancement for visualization, images were processed for segmentation of pores. A median filter and an open-close morphological operator were performed sequentially to reduce noises. Binary images were then created after auto thresholding for dark objects. The areas of pores in terms of pixels were measured by "integrated measurement analysis" function after enabling the "hole filling" function. Porosity of protein matrices was calculated as the percentage of pixel number occupied by pores to the total pixel number in the whole image.

Biodegradation of Protein Pillars: An array of 196 (14 × 14) BSA protein micropillars with dimensions of 2 μm (L) × 2 μm (W) × 10 μm (H) were soaked in fibroblast growth medium, defined as Dulbecco's modified Eagle's medium with high glucose (DMEM-HG) (Gibco, Grand Island, NY), fetal bovine serum (FBS) (10%), P/S (Gibco) (1%), and L-glutamine (Gibco) (2 mM), and incubated at 37 °C, in a CO_2 (5%) incubator. Micropillar arrays were fixed and processed as previously described for SEM analysis at Day 1, 3, 7, and 10, respectively. Ten micropillars were randomly selected from each array for analysis. Image J was used to measure the dimensions (height and width) of the micropillars.

Cytocompatibility Study Using Fibroblasts: Prior to fabricating protein micropillar arrays for cytocompatibility study, protein microwells were fabricated on a culture dish with a glass coverslip at the center. The microwell acts as an isolator separating cells seeded on the pillars and those on the glass. Microwells measured 240 μm (L) x 50 μm (W) x 50 μm (H) were fabricated by *z*-stack scanning with 102 slices in total. The interval between adjacent slices is also 0.5 μm. Parameters including exposure power at 110 mW, pixel dwell time of 1.58 μs were used. The total scan time for a microwell is about 140 s. Four arrays of micropillar were then fabricated within each microwell before seeding fibroblasts. Using autofocus function in microscope in reflection mode to find the interface between solution and glass. Fabrication of micropillars was started from 1 μm below this interface (optimized from previous study) by *z*-stack scanning with 52 slices in total. The interval between adjacent slices is 0.5 μm. Parameters including exposure power at 90 mW and pixel dwell time of 0.79 μs were used. The total scan time for each array is about 20 s. Therefore, the total scan time for fabricating one microwell and four micropillar arrays for a single culture experiment (regarded as one sample) was less than four minutes. After rinsing the dish with DI water three times, each five minutes, samples were sterilized by soaking in ethanol (70%) for 30 min. Mouse 3T3 fibroblasts (ATCC) were subcultured to passage 10 in growth medium. An aliquot of 3.33E4 cells in growth medium was seeded directly onto each coverslip with two microwells and cultured at 37 °C in a humidified atmosphere with CO_2 (5%) with medium replenishment every three to four days. Live and Dead assay was conducted and samples were fixed and processed for SEM analysis at 1, 3, 7, and 10 d. In brief, calcein AM (2 μL) and ethidium homodimer-1 (1 μL) were diluted in DMEM-LG (1 mL) with cells, which were incubated in the dye solution for 45 min at 37 °C. Then cells were washed in phosphate buffered saline (PBS) three times for five minutes.

Expression of Cell Matrix Adhesion Molecules and Deposition of Extracellular Matrix: Fibroblasts seeded micropillar arrays were cultured for one day and seven days for evaluation of cell matrix adhesion molecules and extracellular matrix components, respectively. In brief, samples were fixed at paraformaldehyde (PFA) (4%) for 20 min at room temperature. After three washes with PBS, samples were blocked in BSA (3%) for 30 min. For paxillin staining, samples were permeablized with Tween-20 (0.5%) for 10 min and washed three times before blocking. After blocking, samples were briefly washed with PBS and incubated in primary antibodies (integrin α_v (1:300, ab16821, abcam), integrin β_1 (1:300, ab30394, abcam), paxillin (1:30, AF4259, R&D systems), vitronectin (1:100, ab113700, abcam), collagen (1:1000, C2456, Sigma), and fibronectin (1:300, sc9068, Santa Cruz)) overnight at 4 °C. After three washes with Tween-20 in PBS (0.05%), samples were incubated with Alex-fluor 647 conjugated secondary antibody (Invitrogen, 1:400) for one hour. Samples were then washed three times with Tween-20 in PBS (0.05%) and mounted in Fluro-gel II (EMS) with DAPI. *Z*-stack images were acquired at ≈0.45 μm interval by a CLSM system (Zeiss LSM710) at 63× magnification (Plan-Apchromat 63×/1.4 N.A. objective). 3D images were visualized, analyzed, and captured by Imaris (Bitplane).

Statistical Analysis: All quantitative data were presented in box plots. Regression analysis with linear or quadratic contrast was conducted to reveal the association between various parameters and voxel dimension or matrix porosity. SPSS 19.0 was used to execute all statistical analyses and the significance level was set at 0.05.

Supporting Information

Supporting Information is available from the Wiley Online Library or from the author.

Acknowledgements

J. N. Ma and J. Y. Xu contributed equally to this work. This work was supported by University Development Fund, Strategic Research Themes on Biomedical Engineering and Nanobiotechnology, The University of Hong Kong (HKU). The authors thank the colleagues in the EM unit of the University for assisting the SEM analysis.

Received: February 26, 2013
Revised: June 7, 2013
Published online: July 16, 2013

---

[1] G. M. Gratson, M. Xu, J. A. Lewis, *Nature* **2004**, *428*, 386.
[2] M. Campbell, D. N. Sharp, M. T. Harrison, R. G. Denning, A. J. Turberfield, *Nature* **2000**, *404*, 53.
[3] D. S. Ginger, H. Zhang, C. A. Mirkin, *Angew. Chem. Int. Ed.* **2004**, *43*, 30.
[4] D. Qin, Y. Xia, G. M. Whitesides, *Nat. Protoc.* **2010**, *5*, 491.
[5] A. Biswas, I. S. Bayer, A. S. Biris, T. Wang, E. Dervishi, F. Faupel, *Adv. Colloid Interface Sci.* **2012**, *170*, 2.
[6] C. N. LaFratta, J. T. Fourkas, T. Baldacchini, R. A. Farrer, *Angew. Chem. Int. Ed.* **2007**, *46*, 6238.
[7] K. Salaita, Y. Wang, C. A. Mirkin, *Nat. Nanotechnol.* **2007**, *2*, 145.
[8] V. N. Truskett, M. P. Watts, *Trends Biotechnol.* **2006**, *24*, 312.
[9] K. S. Lee, R. H. Kim, D. Y. Yang, S. H. Park, *Prog. Polym. Sci.* **2008**, *33*, 631.
[10] G. Kumi, C. O. Yanez, K. D. Belfield, J. T. Fourkas, *Lab Chip* **2010**, *10*, 1057.
[11] W. R. Zipfel, R. M. Williams, W. W. Webb, *Nat Biotechnol* **2003**, *21*, 1369.
[12] H. B. Sun, T. Tanaka, S. Kawata, *Appl. Phys. Lett.* **2002**, *80*, 3673.
[13] H. B. Sun, K. Takada, M. S. Kim, K. S. Lee, S. Kawata, *Appl. Phys. Lett.* **2003**, *83*, 1104.
[14] D. Wu, S. Z. Wu, S. Zhao, J. Yao, J. N. Wang, Q. D. Chen, H. B. Sun, *Small* **2013**, *9*, 760.
[15] D. C. Pregibon, M. Toner, P. S. Doyle, *Langmuir* **2006**, *22*, 5122.
[16] S. Seiffert, J. Dubbert, W. Richtering, D. A. Weitz, *Lab Chip* **2011**, *11*, 966.
[17] J. D. Pitts, A. R. Howell, R. Taboada, I. Banerjee, J. Wang, S. L. Goodman, P. J. Campagnola, *Photochem. Photobiol.* **2002**, *76*, 135.
[18] S. Basu, P. J. Campagnola, *Biomacromolecules* **2004**, *5*, 572.

© 2013 WILEY-VCH Verlag GmbH & Co. KGaA, Weinheim

[19] S. Basu, P. J. Campagnola, *J. Biomed. Mater. Res., Part A* **2004**, *71A.*, 359.
[20] B. Kaehr, R. Allen, D. J. Javier, J. Currie, J. B. Shear, *Proc. Natl. Acad. Sci. U. S. A.* **2004**, *101*, 16104.
[21] Y. L. Sun, D. X. Liu, W. F. Dong, Q. D. Chen, H. B. Sun, *Opt. Lett.* **2012**, *37*, 2973.
[22] Y. L. Sun, W. F. Dong, R. Z. Yang, X. Meng, L. Zhang, Q. D. Chen, H. B. Sun, *Angew. Chem. Int. Ed.* **2012**, *51*, 1558.
[23] S. Basu, L. P. Cunningham, G. D. Pins, K. A. Bush, R. Taboada, A. R. Howell, J. Wang, P. J. Campagnola, *Biomacromolecules* **2005**, *6*, 1465.
[24] G. D. Pins, K. A. Bush, L. P. Cunningham, P. J. Campagnola, *J. Biomed. Mater. Res., Part A* **2006**, *78*, 194.
[25] X. Chen, M. A. Brewer, C. Zou, P. J. Campagnola, *Integr. Biol.* **2009**, *1*, 469.
[26] R. Allen, R. Nielson, D. D. Wise, J. B. Shear, *Anal. Chem.* **2005**, *77*, 5089.
[27] P. J. Su, Q. A. Tran, J. J. Fong, K. W. Eliceiri, B. M. Ogle, P. J. Campagnola, *Biomacromolecules* **2012**, *13*, 2917.
[28] B. Kaehr, J. B. Shear, *Proc. Natl. Acad. Sci. U. S. A.* **2008**, *105*, 8850.
[29] B. Kaehr, J. B. Shear, *Lab Chip* **2009**, *9*, 2632.
[30] R. Nielson, B. Kaehr, J. B. Shear, *Small* **2009**, *5*, 120.
[31] J. C. Harper, S. M. Brozik, C. J. Brinker, B. Kaehr, *Anal. Chem.* **2012**, *84*, 8985.
[32] V. Karageorgiou, D. Kaplan, *Biomaterials* **2005**, *26*, 5474.
[33] R. J. DeVoe, H. Kalweit, C. A. Leatherdale, T. R. Williams, in *Materials, theory and applications, Proceedings of SPIE. 4797* (Eds: K. D. Belfield, S. J. Caracci, F. Kajzar, C. M. Lawson, A. T. Yeates), SPIE, Bellingham **2003**, p 310.
[34] A. B. Abell, K. L. Willis, D. A. Lange, *J. Colloid Interface Sci.* **1999**, *211*, 39.
[35] B. Richards, E. Wolf, *Proc. R. Soc. London, Ser. A* **1959**, *253*, 358.
[36] S. Guldbrand, C. Simonsson, M. Smedh, M. B. Ericson, in *Advanced Microscopy Techniques. Proceedings of SPIE-OSA Biomedical Optics. 7367* (Eds: P. J. Campagnola, E. H. K. Stelzer, G. V. Bally), SPIE, Bellingham **2009**, p R1.
[37] D. R. Larson, W. R. Zipfel, R. M. Williams, S. W. Clark, M. P. Bruchez, F. W. Wise, W. W. Webb, *Science* **2003**, *300*, 1434.
[38] M. Miwa, S. Juodkazis, T. Kawakami, S. Matsuo, H. Misawa, *Appl Phys A* **2001**, *73*, 561.
[39] C. A. Leatherdale, R. J. DeVoe, in *Nonlinear optical transmission and multiphoton processes in organics. Proceedings of SPIE. 5211* (Eds: A. D. Yeates, K. D. Belfield, F. Kajzar, C. M. Lawson), SPIE, Bellingham **2003**, p 112.
[40] S. Kawata, H. B. Sun, T. Tanaka, K. Takada, *Nature* **2001**, *412*, 697.
[41] J. M. Mann, R. H, Lam, S. Weng, Y. Sun, J. Fu, *Lab Chip* **2012**, *12*, 731.
[42] R. H. Lam, Y. Sun, W. Chen, J. Fu, *Lab Chip* **2012**, *12*, 1865.
[43] B. K. Teo, K. J. Goh, Z. J. Ng, S. Koo, E. K. Yim, *Acta Biomater.* **2012**, *8*, 2941.
[44] M. T. Yang, D. H. Reich, C. S. Chen, *Integr. Biol.* **2011**, *3*, 663.
[45] W. R. Legant, J. S. Miller, B. L. Blakely, D. M. Cohen, G. M. Genin, C. S. Chen, *Nat. Methods* **2010**, *7*, 969.
[46] S. K. Seidlits, C. E. Schmidt, J. B. Shear, *Adv. Funct. Mater.* **2009**, *19*, 3543.
[47] S. Basu, C. W. Wolgemuth, P. J. Campagnola, *Biomacromolecules* **2004**, *5*, 2347.
[48] E. Cukierman, R. Pankov, K. M. Yamada, *Curr. Opin. Cell Biol.* **2002**, *14*, 633.

© 2013 WILEY-VCH Verlag GmbH & Co. KGaA, Weinheim